Numerical Simulation of the Arctic Ocean Circulation

ALBERT J. SEMTNER, JR.

Department of Meteorology, University of California, Los Angeles 90024

(Manuscript received 13 October 1975, in revised form 27 January 1976)

ABSTRACT

The circulation of the Arctic Ocean and Greenland Sea is simulated using the 1969 numerical model of Bryan and Cox. The coastline and bottom topography of the region are resolved by a 110 km horizontal grid spacing and by 14 vertical levels. The transfers of mass, heat and momentum at the ocean surface and at open lateral boundaries are specified from observations. In particular, the pattern of wind stress is obtained using a map of mean annual atmospheric pressure; and a scalar multiplier is applied to account for the nonlinear dependence of stress on wind speed. Three experiments with different values of this scalar multiplier are run to simulate the effect of high, medium and low wind stress. The first experiment is carried out for the combined Arctic Ocean and Greenland Sea, while the other two experiments are run for the Arctic Ocean only.

Many of the observed features of the Arctic circulation are reproduced by the simulations. The Greenland Sea exhibits cyclonic flow at all levels and deep convection in its central region. The Beaufort Sea shows anticyclonic flow at the surface and a stable stratification maintained by a halocline. The Arctic Ocean receives bottom water and an intermediate layer of warm Atlantic water through the Greenland-Spitsbergen Passage, and it exports surface water of low salinity into an intense East Greenland Current. The sense of circulation of the Atlantic layer in the central Arctic Ocean, although opposite to that usually inferred from water mass properties, seems to be in reasonable agreement with existing direct current measurements.

For computational reasons, an excessively large eddy viscosity is required in the experiments. As a result, predicted currents are too weak unless a large wind stress is used, but then an excessive Ekman pumping makes the halocline too deep and erodes the temperature maximum in the Atlantic layer. These results indicate that simulations with finer resolution and reduced viscosity should be more realistic.

1. Introduction

The Arctic Ocean and Greenland Sea are important areas of the world ocean. The Greenland Sea is thought to produce most of the bottom water which drives the North Atlantic thermohaline circulation, whereas the Arctic Ocean strongly influences the heat budget of the Northern Hemisphere by providing stably stratified surface water on which sea ice can form. Both regions may be sensitive to climatic variations on account of positive feedback mechanisms associated with the formation of sea ice. Together, they constitute a natural sub-portion of the world ocean, whose exchanges with the remainder of the ocean can be monitored across relatively narrow and shallow ridges. Thus both the potential climatic importance and the relatively closed geometry of the Arctic Ocean and Greenland Sea provide good reasons to single out the area for dynamical study.

One method of understanding oceanic dynamics is to simulate the circulation with a numerical model. Such an approach is especially valuable for polar regions, where oceanic observations are hindered by bad weather and by the presence of sea ice. Given a perfect ocean model and perfect boundary conditions, one could numerically simulate the circulation and then analyze the dynamical processes.

Unfortunately, neither a perfect ocean model nor a perfect set of observed boundary data are available at this time. The principal limitation on modeling is that of low spatial resolution which must be used in long-term integrations. This forces the use of unrealistically large eddy viscosity to suppress computational noise in poorly resolved wavenumbers. Observations of atmospheric forcing are also limited, especially in polar regions. Only mean annual forcing and regional budget values are known with some degree of certainty. But even with these limitations, an improved understanding of the three-dimensional Arctic circulation may still be gained by numerical simulations.

Previous studies on Arctic circulation have been mainly two-dimensional. Numerical studies have been made by Campbell (1965) and Galt (1973). Recently, a two-layer analytical study has been carried out by Hart (1975). The present work is, to the author's knowledge, the first three-dimensional long-term simulation of Arctic circulation, as driven by observed atmospheric forcing. A detailed description of the predicted fields and analysis of the governing dynamics is avail-

able in the author's Ph.D. dissertation (Semtner, 1973). This paper presents the most important predicted fields from that study.

2. Description of the model

The basic tool used in this study is the numerical ocean model of Bryan and Cox (cf. Bryan, 1969). The governing equations are

$$\frac{\partial \mathbf{v}}{\partial t}+\mathbf{v}\cdot\nabla_H\mathbf{v}+w\frac{\partial \mathbf{v}}{\partial z}+f(\mathbf{k}\times\mathbf{v}) = -\frac{1}{\rho_0}\nabla_H p+K\frac{\partial^2\mathbf{v}}{\partial z^2}+A_M\nabla_H^2\mathbf{v}$$

$$\frac{\partial p}{\partial z}=-\rho g$$

$$\nabla_H\cdot\mathbf{v}+\frac{\partial w}{\partial z}=0$$

$$\frac{\partial}{\partial t}(T,S)+\mathbf{v}\cdot\nabla_H(T,S)+w\frac{\partial}{\partial z}(T,S) = K\frac{\partial^2}{\partial z^2}(T,S)+A_H\nabla_H^2(T,S)$$

$$\rho=\rho(T,S,z).$$

In the above, the variables $\mathbf{v}$, w, p, T, S, ρ represent horizontal velocity, vertical velocity, pressure, potential temperature, salinity and density, respectively. The horizontal momentum equations are retained in relatively complete form, with subgrid processes parameterized via a constant vertical eddy viscosity $K=0.3$ cm^2 s^{-1} and a constant horizontal eddy viscosity $A_M=4\times10^8$ cm^2 s^{-1}. (Although the former constant is of a physically realistic magnitude, the latter is unrealistically high, but is chosen as such for computational reasons.) The vertical momentum equation is approximated by the hydrostatic equation, and the ocean is taken to be incompressible. Heat and salt are transported by the large-scale currents and assumed to diffuse by subgrid-scale eddy diffusion, using $A_H=10^7$ cm^2 s^{-1}. (The value for A_H is also chosen to supress computational noise, and may be physically too large.) Density is computed from an empirical equation of state (cf. Bryan and Cox, 1972). Finally, because hydrostatic balance is assumed, convective adjustment is employed in the model whenever the vertical density structure would be gravitationally unstable.

The vertical exchange coefficient $K=0.3$ cm^2 s^{-1} was able to be specified freely, without regard for the suppression of computational noise. In previous numerical experiments a value $K=1.0$ cm^2 s^{-1} has often been used, in accordance with early observational evidence on the vertical distribution of trace substances. Typically, the numerically predicted thermocline depths have been larger than in the real ocean. This indicates that a reduced value of K may be more realistic; and, in fact, observational evidence by Rooth and Östland (1972) suggests a value closer to 0.2 cm^2 s^{-1}.

The use of a small K may underestimate vertical exchanges in those oceanic regions where baroclinic eddies provide additional mixing over that due to small-scale turbulence. In a model having sufficiently high resolution, such eddies would be explicitly resolved. In this study, such eddies are suppressed, and thus vertical mixing in certain regions may be misrepresented. The value of K may also seem unrealistically small for mixing processes near the ocean surface; but this is not a serious problem, because the finite-difference budget equations treat the uppermost model layer as a *de facto* mixed layer of constant depth within which K may be considered very large.

The governing equations are solved in finite-difference form for an ocean of arbitrary geometry. Readers interested in the details may consult Bryan (1969) or Semtner (1974). It suffices here to note that (i) an energetically consistent scheme with second-order accuracy is used; (ii) a rigid-lid approximation is used to suppress external gravity waves and thereby allow a longer timestep; and (iii) other transient motions are filtered by a method of Bryan *et al.* (1975), which speeds adjustment of density and velocity to a steady state. In order to study a polar basin without encountering coordinate singularities, an unusual spherical coordinate system is chosen, with its equator and prime meridian running through the earth's rotational pole. The vertical component f of the Coriolis acceleration then becomes a function of both longitude λ and latitude φ in the new coordinate system, i.e.,

$$f=2\Omega\cos\lambda\cos\varphi.$$

Fig. 1 shows the horizontal layout of the grid. Increments of 1° in λ and φ give a horizontal grid spacing of approximately 110 km. Centers of grid points on land are denoted by small squares. Some geographical names are indicated, and circles of the geographical latitude are also shown. Spitsbergen and Iceland are included as true islands in the model, while several island groups offshore from Russia are treated as extensions of the mainland. Fig. 2 shows a contour map of the bottom topography, as represented by the 14 levels of the model. Grid-box thicknesses increase from 15 m near the surface to 600 m near the abyssal plains. The prominent Lomonosov Ridge separating the Canadian and Eurasian portions of the deep Arctic Basin is explicitly resolved, as is the sill between the Eurasian and Greenland basins. Bathymetric data of Smith *et al.* (1965) were used to construct the model topography.

Lateral boundary conditions are needed for the computation. At solid walls, no-slip conditions for momentum and no-flux conditions for heat and salt

are used. At the open boundaries of the region, observed values of temperature, salinity and velocity are specified. Data on temperature and salinity are obtained (i) for the Bering Strait from Coachman and Aagaard (1966), (ii) for McClure Strait and Robeson Channel using Beaufort Sea values from Coachman and Aagaard (1974), (iii) for the Denmark Strait from Dietrich (1960), and (iv) for the Faeroe-Shetland Channel from Worthington (personal communication). At open boundaries the vertical shear of velocity is computed from specified densities using the thermal wind relation, whereas the vertical mean velocity is specified on the basis of estimated mass transports. A volume transport of 10^6 m^3 s^{-1} inward through the Bering Strait is assumed, with 0.5×10^6 m^3 s^{-1} out through both the McClure Strait and the Robeson Channel. [These are minimum transport estimates of Aagaard (personal communication).] An inflow of 7×10^6 m^3 s^{-1} is prescribed for the Faeroe-Shetland Channel, with an equal amount of outflow through the Denmark Strait. [Worthington (1970) estimates 8×10^6 m^3 s^{-1} for each.]

Case I is a simulation of the circulation in the combined Arctic Ocean and Greenland Sea. For Cases II and III, only the central Arctic Basin is treated. In those two cases, the temperature, salinity and velocity are specified along a section from Russia to Spitsbergen using the results of Case I, and specified across the Greenland-Spitsbergen Passage using data from Palfrey (1967) and the National Oceanographic Data Center. Table 1 shows the values used across the last passage. Tabulated values for the other passages are given in Semtner (1973).

Momentum flux must be specified at the surface of the ocean. In the central Arctic Basin, momentum is transmitted to the ocean primarily by the motion of the overlying sea ice. If an observed field of long-term drift velocities of ice were available, one could specify the stress on the ocean as a function of the difference be-

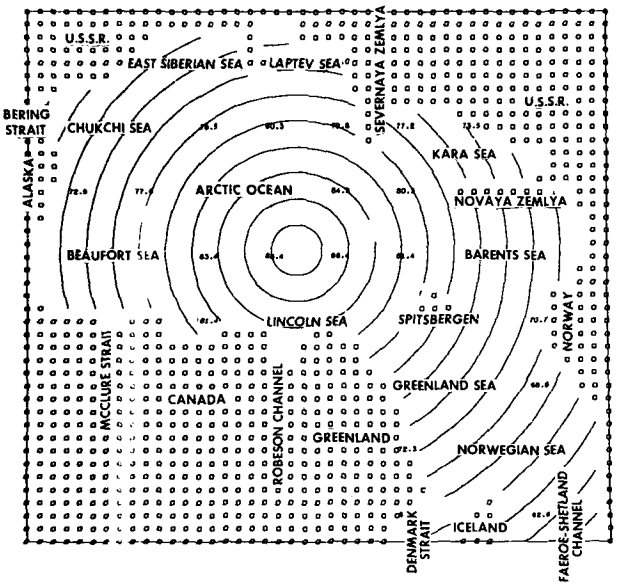

FIG. 1. Geographical features represented in the numerical grid. Small squares indicate centers of grid points on land. Latitude circles every 2° are shown.

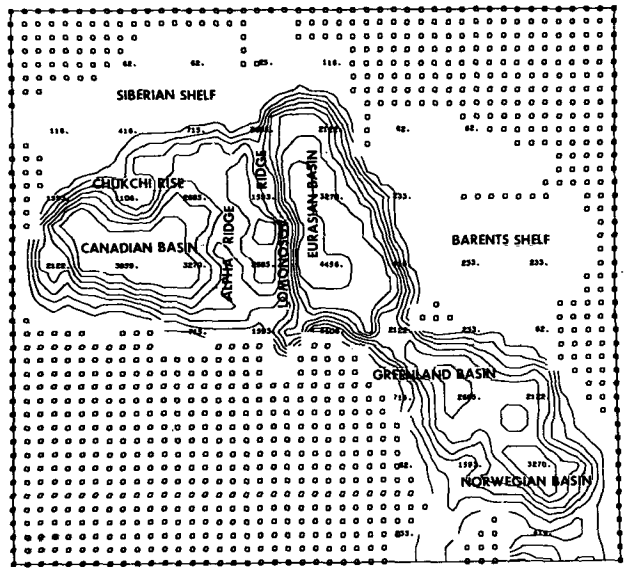

FIG. 2. Prominent bathymetric features, as resolved by depths specified in the model. The contour interval is 500 m.

TABLE 1. T, S and v for the Greenland-Spitsbergen Passage. Temperature (°C) and salinity (‰) are given in each grid box. Normal velocity (cm s^{-1}) is shown on the common edge between two boxes. The section is viewed from the south, with positive velocities denoting flow into the Arctic Basin. Grid-point depths are shown at the left.

Depth (m)									
7.5	−0.90		−1.13		+2.00		+4.99		
	30.60	−10.0	30.40	−8.58	33.87	+3.50	34.65		
20	−1.03		−1.25		+1.60		+5.25		
	31.13	−9.93	31.65	−7.32	34.25	+3.62	34.83		
44	−1.60		−1.60		+1.35		+5.26		
	32.80	−9.60	33.05	−5.76	34.55	+3.60	34.83		
90	−1.66		−1.57		+1.20		+4.70		
	33.95	−9.34	34.03	−4.23	34.80	+3.31	35.04		
175	−0.30		+0.10		+1.91		+3.35		
	34.50	−9.16	34.57	−2.96	34.99	+2.92	35.07		
325			+1.20		+1.62		+2.32		
			34.91	−2.08	35.03	+2.55	35.50		
565			+0.30		+0.88		+1.30		
			34.88	−1.40	35.02	+2.12	35.02		
910			−0.13		−0.21		−0.50		
			34.89	−0.49	34.95	+2.02	34.95		
1350			−0.47		−0.71				
			34.90	+0.45	34.93				
1860			−0.71		−0.87				
			34.91	+1.45	34.95				

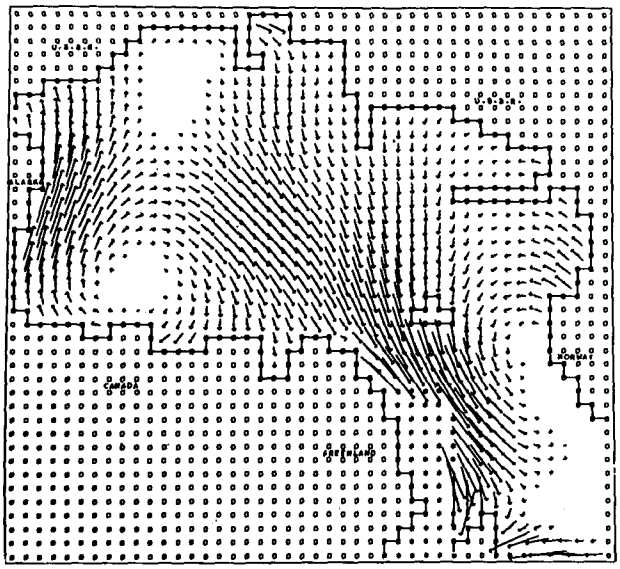

FIG. 3. Wind stress computed from mean annual atmospheric pressure maps. The distance between grid points gives a scale of 0.13 dyn cm^{-2}. Stresses due to enhanced winds paralleling the eastern margin of the Greenland ice cap are not shown.

tween observed ice velocity and predicted water velocity, using an empirically determined drag coefficient. However, only the major features of ice drift are known; and it seems necessary to fall back on a field with better spatial definition—the wind stress itself. Several investigators have recently expressed the opinion that the long-term forcing of wind on sea ice is transmitted to the water beneath the ice with little modification (Coachman and Aagaard, 1974; Galt, 1973). We assume that is the case for this study, since a full description of the ice motion or an understanding of how ice modifies the wind stress may not be gained for a number of years. Thus, the wind stress is taken to act directly on the ocean, regardless of ice cover.

Even the determination of wind stress poses problems in polar regions. Direct measurements of surface winds are too sparse to be used, and one must infer winds from atmospheric pressure maps. Synoptic pressure maps may have large errors associated with insufficient data in the central Arctic Basin, and these errors could be magnified by a nonlinear drag law. We use an indirect approach, therefore, involving long-term averages of atmospheric pressure.

To obtain a field of wind stress, mean geostrophic wind velocities $\bar{\mathbf{v}}_g$ (where a bar denotes a time average) are first obtained from available maps of mean annual atmospheric pressure. Stresses due to the average wind are computed using a drag law

$$|\boldsymbol{\tau}| = \rho_{\text{air}}(2\times10^{-3})|\bar{\mathbf{v}}_g|^2$$

and assuming a turning angle of 19° in the atmospheric boundary layer. The drag coefficient is a compromise between a value appropriate for ice-covered regions [2.6×10^{-3} according to Smith (1970)] and a value appropriate for the open ocean [1.3×10^{-3} according to Kraus (1972)]. The drag coefficient is applied directly to the geostrophic wind, since anemometer and geostrophic wind speeds have been observed to be nearly equal over the Greenland Sea (Aagaard, 1969).

A pattern of wind stress due to mean annual winds is shown in Fig. 3. The winds are obtained by smoothly joining together the pressure maps of Fel'zenbaum (1961) for the central Arctic, Dunbar and Wittman (1963) for the Barents and Kara Seas, and Aagaard (1970) for the Greenland Sea. The computed stresses are unrealistically small as they stand, because the mean stress should really be obtained from $|\overline{|\mathbf{v}_g|\mathbf{v}_g}|$ rather than $|\bar{\mathbf{v}}_g|^2$. However, a study by Welch (1972) has shown that these quantities can be approximately related by means of a scalar constant α, dependent mainly on the averaging time, i.e.,

$$|\overline{|\mathbf{v}_g|\mathbf{v}_g}| = \alpha|\bar{\mathbf{v}}_g|^2.$$

Welch computed wind-driven ocean transports in the North Pacific using both synoptic pressure maps and monthly average pressure maps; and his results (see Fig. 4) indicate that a factor $\alpha=4$ would work reasonably well with monthly average maps. When mean annual pressure maps are employed, α should be even larger. In this study, we treat α as a parameter, and use values of 15, 8 and 1.5 for Cases I, II and III, respectively. In this way, we also explore the response of the Arctic Ocean to different relative amounts of wind forcing and thermohaline forcing.

A surface boundary condition is needed for the heat equation. The ocean surface temperature is often specified in numerical experiments. This would seem appropriate for the ice-covered regions of the central Arctic, where temperatures remain near the freezing point throughout the year and seasonal variations in heat flux are buffered by relatively small (~50 cm) changes in ice thickness. However, in the predominantly ice-free Greenland and Norwegian Seas, a specification of ocean surface temperature could cause excessive heat losses from the ocean due to unrealistically large convective overturning (cf. Holland, 1971). In these regions, a flux condition would be better from a physical standpoint.

In this experiment, a boundary condition is used which seems appropriate for both the central Arctic and the Greenland Sea. Large negative heat flux values, appropriate to an ice-free polar area, are applied whenever the surface temperature in the model ocean is above −2°C. However, if the temperature drops below −2°C at any grid point, a very small heat loss, appropriate for ice-covered regions, is used there. This simulates the formation of an insulating ice cover and tends to keep the temperature near the freezing point. In this way, the exact region covered by ice is not

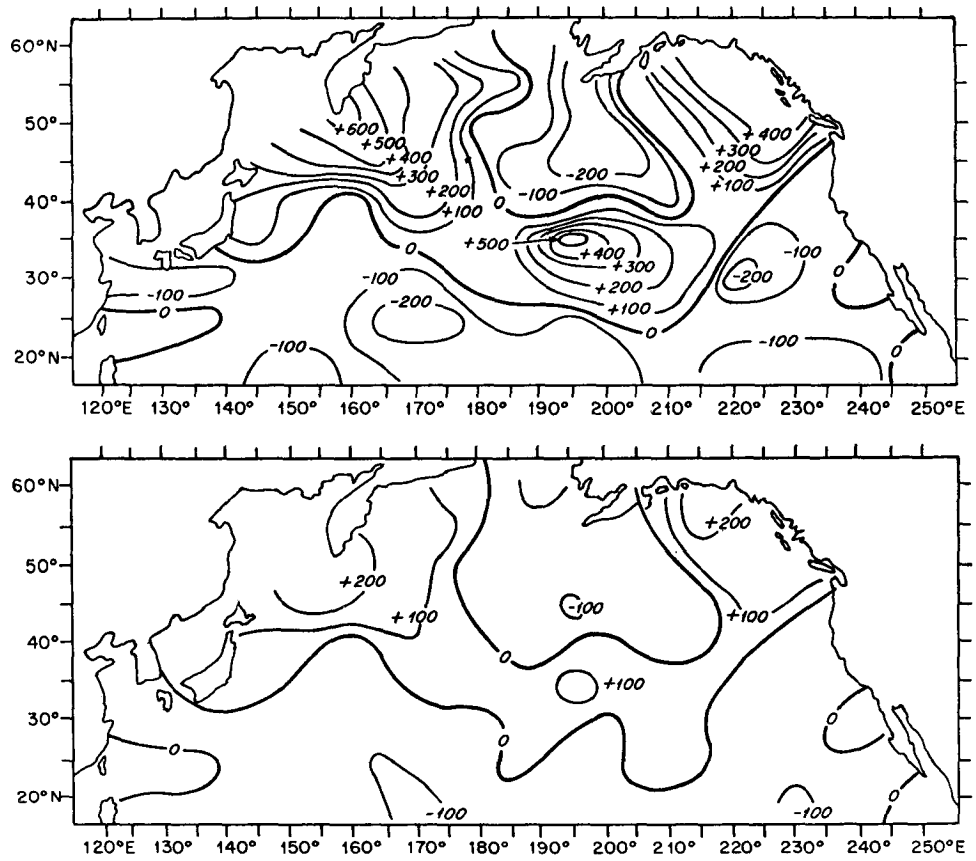

FIG. 4. Patterns of wind-driven (Sverdrup) transport in the North Pacific, as computed from synoptic maps of surface atmospheric pressure (top) and as computed from a monthly average map of atmospheric pressure (bottom), according to Welch (1972).

specified in advance, but emerges as part of the prediction.

Estimates of oceanic heat flux based on the heat budget of sea ice in the central Arctic have been summarized by Maykut and Untersteiner (1969). A typical estimate is 1.6 kcal cm^{-2} $year^{-1}$. This value for negative heat flux is used in the model whenever the ocean surface temperature is $-2°C$ or lower.

Several estimates of oceanic heat flux are available for the Norwegian and Greenland Seas. Budyko (1963) charts the residual of radiative and turbulent energy fluxes and shows an average heat loss of about 60 kcal cm^{-2} $year^{-1}$. Worthington (1970) estimates a surface loss of 75 kcal cm^{-2} $year^{-1}$, based on a residual of lateral heat transport by ocean currents. Worthington's value would drop to 64, however, if the warm inflow through the Faeroe-Shetland Channel were 7×10^6 m^3 s^{-1} rather than 8×10^6. To be consistent with a prescribed inflow of 7×10^6 m^3 s^{-1} in the model, we take the heat loss over water above $-2°C$ in temperature to be 64 kcal cm^{-2} $year^{-1}$.

One problem with the use of mean annual heat fluxes is that the temperature of bottom water formed by deep convection will be too high. Convection is a nonlinear process, in that it tends to transmit minimum rather than average surface temperature values to the deep ocean. In Case I only, a fluctuating component of heat flux is added to the mean annual component. Based on estimates of monthly turbulent fluxes in the Greenland Sea (Vowinckel and Taylor, 1964) and of net radiative fluxes in an ice-free polar ocean (Fletcher, 1965), the fluctuating component is taken to have a negative cosine dependence on yearly phase angle and twice the amplitude of the mean component. This fluctuation is applied only in the Greenland, Norwegian and Barents Seas for Case I. The fluctuation is not applied in the central Arctic, where sea ice inhibits seasonal variability at the ocean surface itself. If a simple thermodynamic sea-ice model were included in the numerical model, seasonal variations in heat flux from the atmosphere could be prescribed over the entire area. A simple sea-ice model has been developed subsequent to these simulations (cf. Semtner, 1976), and could be included in future studies.

A surface boundary condition is needed for the salt equation. Because the present ocean model is of the "rigid-lid" type and does not allow water mass to be added directly at the surface by precipitation or runoff, prescribed fluxes of salt are specified instead. A small amount of water transport ($\sim0.2\times10^6$ m^3 s^{-1}) is

TABLE 2. Configuration of the experiments.

Region studied	Arctic Ocean and Greenland Sea in Case I Arctic Ocean only in Cases II and III
Grid-point spacing	110 km in the horizontal 15 m–600 m in the vertical
Eddy parameters	$K = 0.3$ cm^2 s^{-1} $A_H = 10^7$ cm^2 s^{-1} $A_M = 4 \times 10^8$ cm^2 s^{-1}
Magnitude of wind stress	High for Case I Medium for Case II Low for Case III
Thermal forcing at surface	Heat flux of $\begin{cases} -64 \text{ kcal cm}^{-2} \text{ year}^{-1} \text{ if } T > -2°\text{C} \\ -1.6 \text{ kcal cm}^{-2} \text{ year}^{-1} \text{ if } T \leqslant -2°\text{C} \end{cases}$ plus additional seasonal variation in marginal seas for Case I
Surface hydrological forcing	Runoff from major rivers; additional coastal runoff; 20 cm yearly precipitation less evaporation
Lateral boundary conditions	Exchanges of mass, heat, and salt specified from observations
Integration time	Case I: 107 years Case II: 36 years Case III: 80 years

neglected, but the dominant effect of fresh water exchange on surface density is retained. Fresh water transfer is converted to salt flux at an assumed salt concentration of 35‰.

River runoff into the Arctic Ocean is specified in the following way. Outflow from each of eight major rivers is deposited in the grid box nearest the mouth of the river. Values for runoff (10^3 m^3 s^{-1}) are taken from Lvovitch and Ovtchinnikov (1964):

Mackenzie	7.9	Kolyma	3.8
Ob	12.4	Lena	15.4
Yenisei	17.3	Pechora	4.1
Dvina	3.5	Mezen	0.8

An additional runoff of 74.3×10^3 m^3 s^{-1} is distributed uniformly around the perimeter of the Arctic Ocean and Greenland Sea. This amount can be regarded as coastal runoff from numerous minor rivers, and it brings the total amount of runoff to 139.5×10^3 m^3 s^{-1}, the net amount estimated by Antonov (cf. Timofeyev, 1963).

The excess of precipitation over evaporation in the polar oceans is relatively small. Sverdrup *et al.* (1942) estimate a yearly value of 12 cm for the Arctic Ocean and 50 cm for the Greenland Sea. In the model, a uniform value of 20 cm is prescribed. This contribution is relatively small compared to river runoff, since the yearly runoff would cover the central Arctic with fresh water to a depth of about 100 cm if spread uniformly over that area.

The pertinent features of the three numerical experiments are summarized in Table 2. The most important distinctions to remember are that (i) wind stress magnitudes differ in the three experiments and (ii) Case I includes the Greenland Sea and has a seasonally varying heat flux in that region.

3. Spinup to quasi-equilibrium

Each of the three experiments achieves quasi-equilibrium by long-term integration from a simple initial state. Except at open boundaries, temperature and salinity are initially specified only as functions of depth. Profiles representative of conditions in the mid-Arctic are used. The extent to which these profiles remain unchanged in the mid-Arctic will then be some measure of the accuracy of the prediction. However the initial profiles should not bias the final state, since the experiments are run for many decades. During this time the effect of initial conditions in all but the deepest layers should be erased.

Case I is run for 107 years, but does not fully adjust in the depths of the Canadian and Eurasian Basins. The initial density there is higher than that of the predicted bottom water which is produced in the Greenland Sea and transported through the Greenland-Spitsbergen Passage. The additional time required for

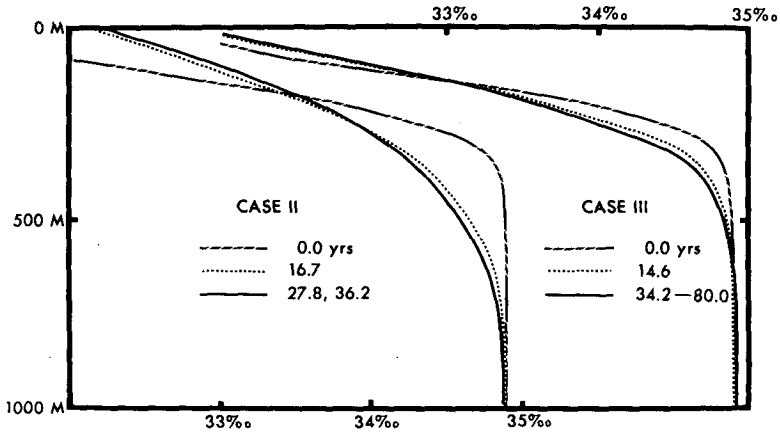

FIG. 5. Time development of vertical salinity profiles in the Eurasian Basin for Cases II and III. The lower scale is for Case II and the upper scale is for Case III.

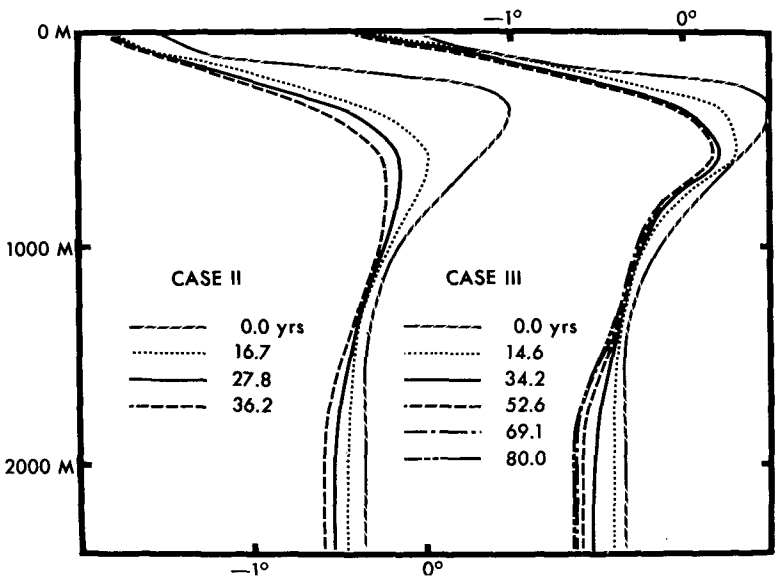

FIG. 6. As in Fig. 5 except for vertical temperature profiles.

vertical diffusion to destroy the slightly stable deep stratification is on the order of a century, so integration to full equilibrium is not attempted. However, in Cases II and III, deep water of somewhat lower density is specified at the beginning, and the deep basins are then flushed out by denser water masses produced at intermediate depths. In these cases, even the deep water attains near-equilibrium.

Figs. 5 and 6 illustrate the time evolution of salinity and temperature for Cases II and III, as monitored in the Eurasian Basin near the North Pole. After 30 years, no significant changes occur in vertical salinity structure. The scale depth of the halocline, which seems to be established in about 15 years, is too large in Case II but just about right in Case III. The thermal adjustment time appears to be about 40 years, so that some slight changes in Case II may still be occurring at the end of the 36-year integration. Case III seems to be

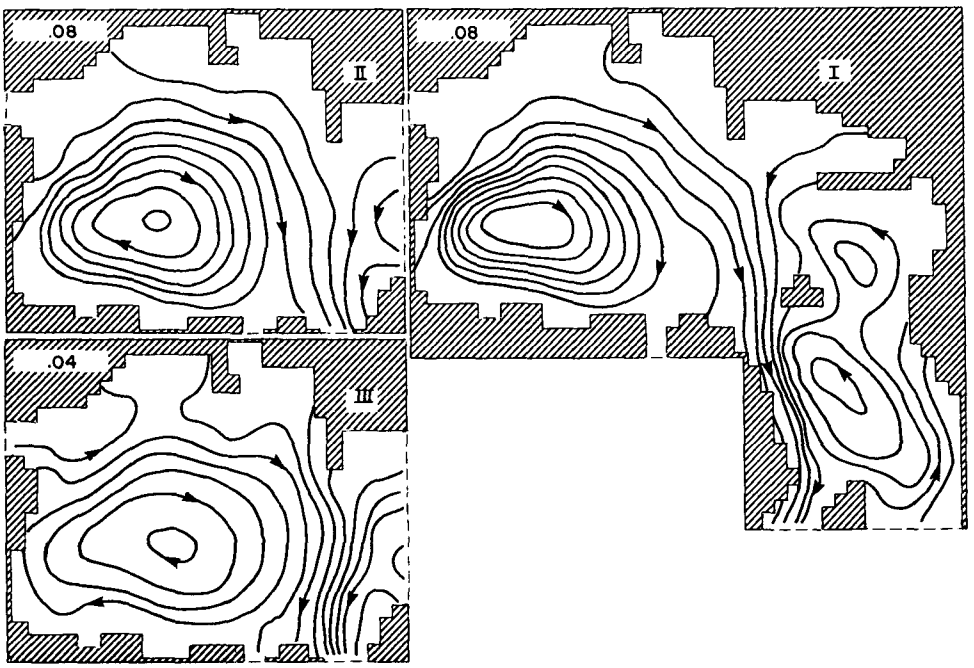

FIG. 7. Predicted pressure fields at 20 m. The contour interval in dynamic meters is shown at the upper left of each frame.

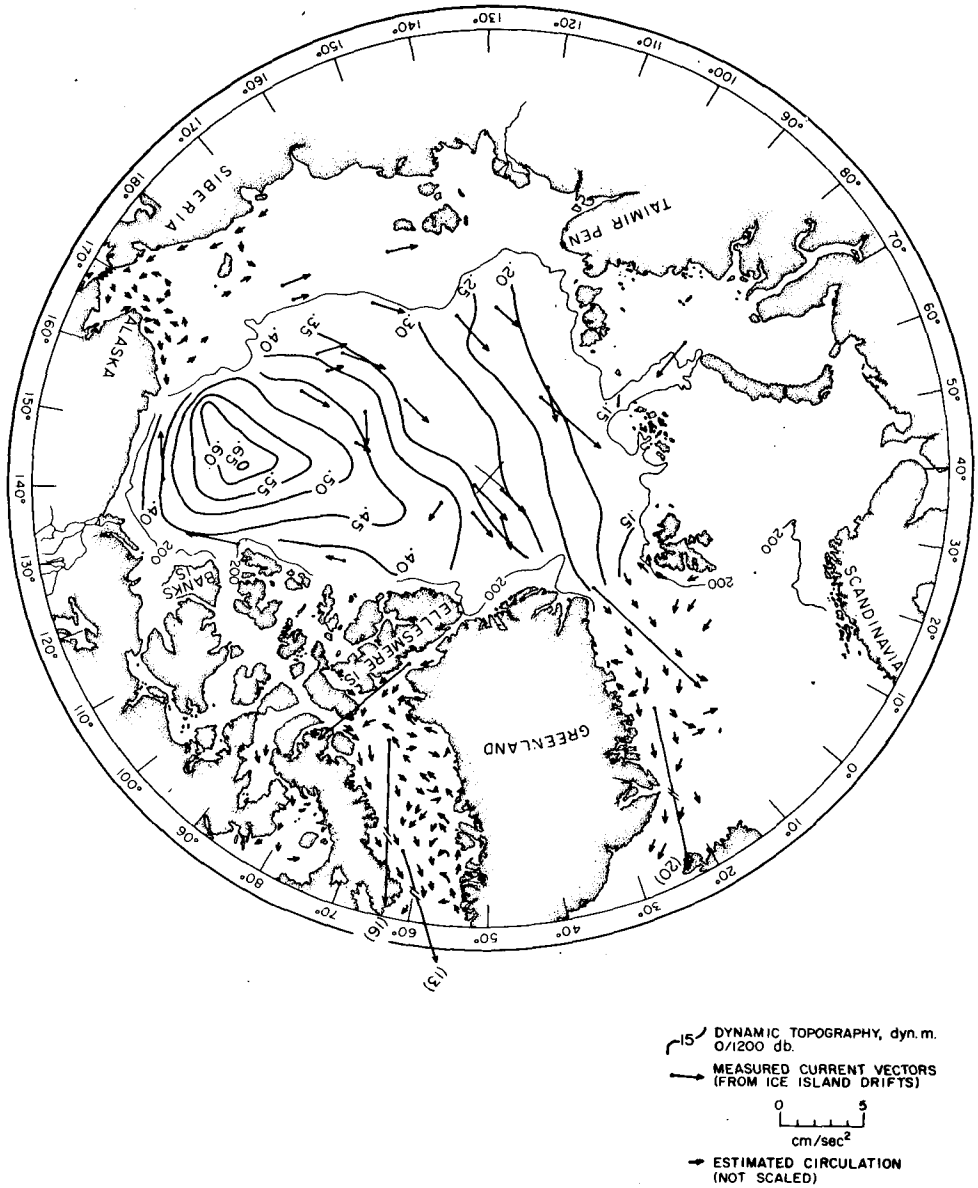

FIG. 8. Observed surface circulation, dynamic topography, and long-term mean station drifts, from Coachman and Aagaard (1974).

quite well adjusted after its 80-year integration and shows a well-defined subsurface temperature maximum consistent with that of the real ocean.

4. Predicted fields of motion

Horizontal flow patterns at a depth of 20 m are shown in Fig. 7. Fields of absolute pressure serve as stream-functions for the highly geostrophic flow. These can be compared with the observed surface circulation, shown in Fig. 8. A number of common features can be noted: 1) a closed circulation in the Canadian Basin, with somewhat intensified flow near the Alaskan Coast; 2) a stagnation point north of Greenland; 3) a Transpolar Drift from the Siberian Shelf toward the Greenland-Spitsbergen Passage; and 4) intense flow in an East Greenland Current. Also, the cyclonic sense of circulation in the Norwegian-Greenland Sea and in the Barents Sea agrees with known surface drift (for example, see U. S. Navy Hydrographic Office, 1958).

The location of the Beaufort Gyre and its general shape for Case I (high wind stress) appear to match those of the observed field best. However velocities are too high by about 50%. Although Case II shows somewhat better current speeds, both it and the noticeably sluggish Case III predict less realistic patterns of flow. These discrepancies are caused mainly by excessive friction, as will be discussed in the last section.

Fig. 9 gives an idea of the circulation at intermediate

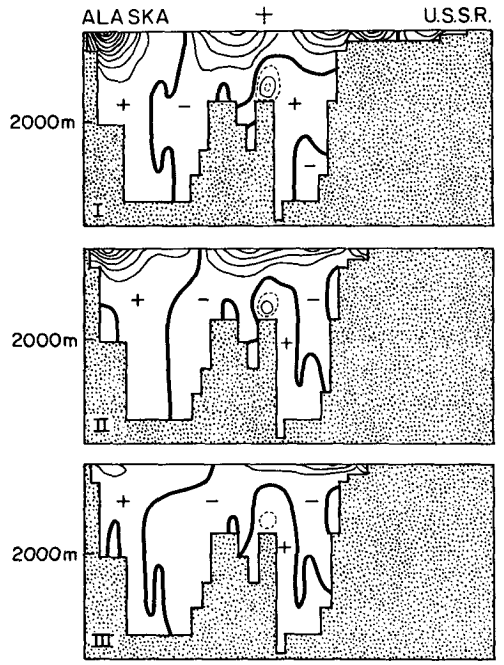

FIG. 9. Predicted velocities normal to a vertical section across the Arctic Basin. The section runs along the 140°W meridian to the pole and continues along the 40°E meridian. Contour interval is 1 cm s^{-1} (except near the top of the Lomonosov Ridge, where 0.5 and 1.5 cm s^{-1} dashed lines are added).

and deep levels in the Arctic Ocean. The normal component of velocity is shown for a vertical section running left to right from Alaska through the North Pole into the Barents Sea. The sense of circulation in the Canadian Basin is anticylonic at all levels and in all experiments. Changes in wind stress mainly affect the strength of the flow. In the Eurasian Basin, the direction of flow near the Barents Shelf seems to be sensitive to whether an interaction with the Greenland Sea is predicted (as in Case I) or prescribed (as in Cases II and III). Near the Lomonosov Ridge, however, similar flows occur in all three cases. The most notable feature is a relatively strong and organized current above the Lomonosov Ridge, moving opposite to the surface current. The depth of current reversal becomes somewhat shallower as wind stress decreases; in Case III, especially, this favors the transport of Atlantic layer water into the Arctic Basin.

A schematic view of the flow in the Atlantic layer (565 m) for Case III is shown in Fig. 10. Anticyclonic gyres exist in the Canadian Basin and in a portion of the Eurasian Basin. A small cyclonic gyre is set up near the Greenland-Spitsbergen Passage. This is a more complicated pattern than that of one large cyclonic gyre, as proposed by Coachman and Barnes (1963) on the basis of water-mass analysis. Some direct current measurements are also shown in Fig. 10 (Coachman and Aagaard, 1974). Reasonable agreement exists between the observed circulation and that of the model. However additional current measurements will be needed in the areas adjacent to the Chukchi Rise, the Canadian Archipelago, and the Barents Shelf, in order to be certain of the actual circulation in the Atlantic layer.

The predicted velocity component normal to a section across the Greenland Sea is shown in Fig. 21 (top). Near the surface, Case I predicts both a northward-flowing Norwegian Current with an offshore maximum and an intense southward-flowing East Greenland Current concentrated near the coast. At deeper levels, the sense of circulation remains the same as at the surface. In fact, a single gyre tends to fill the area of the Greenland and Norwegian Basins. All of these features are in reasonable agreement with existing observations (Coachman and Aagaard, 1974).

Streamfunctions of vertically integrated volume transport are shown in Fig. 11. Most of the water transport is confined to the deep basins. A cyclonic gyre in the Greenland Sea and an anticyclonic gyre in the Canadian Basin have the same sense as the driving wind stress. As wind stress decreases, there is a tendency for an additional gyre to develop in the Eurasian Basin.

Vertical velocities at the base of the uppermost layer (15 m) are shown in Fig. 12. In the interior, the effect of wind curl dominates through Ekman pumping or suction. Near lateral boundaries, strong flow of opposite sign usually occurs to compensate the interior mass flux.

As we shall see later, the vertical velocity at the base

FIG. 10. Schematic view of Atlantic layer circulation (dashed arrows) predicted by Case III of the model, with direct current measurements (solid arrows) compiled by Coachman and Aagaard (1974). The velocity scale at the lower right is for the observed currents.

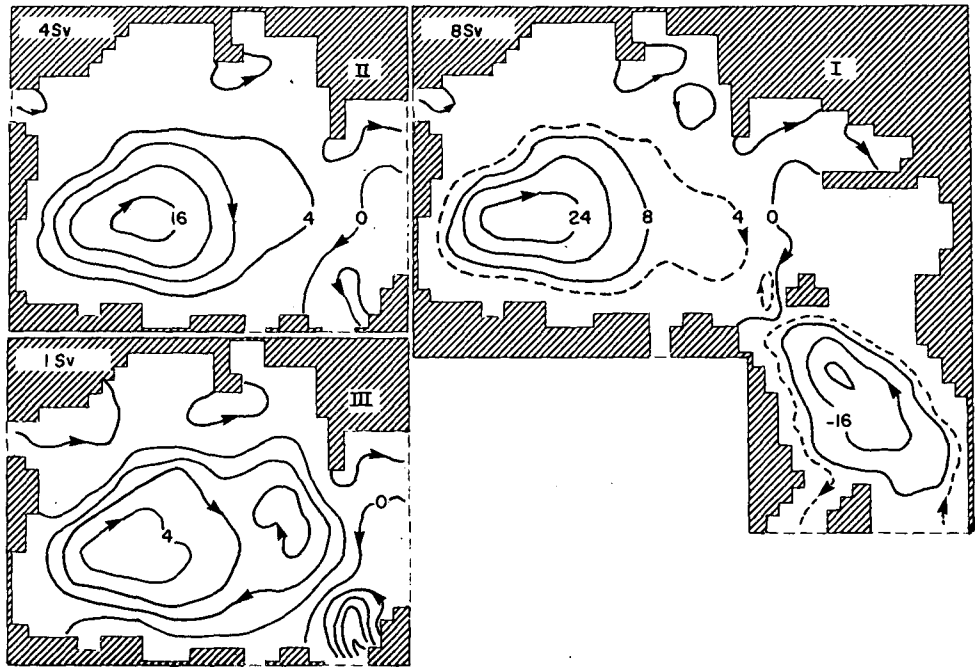

FIG. 11. Streamfunctions of vertically integrated transport. On each frame, the contour interval in units of 10^6 m^3 s^{-1} is shown.

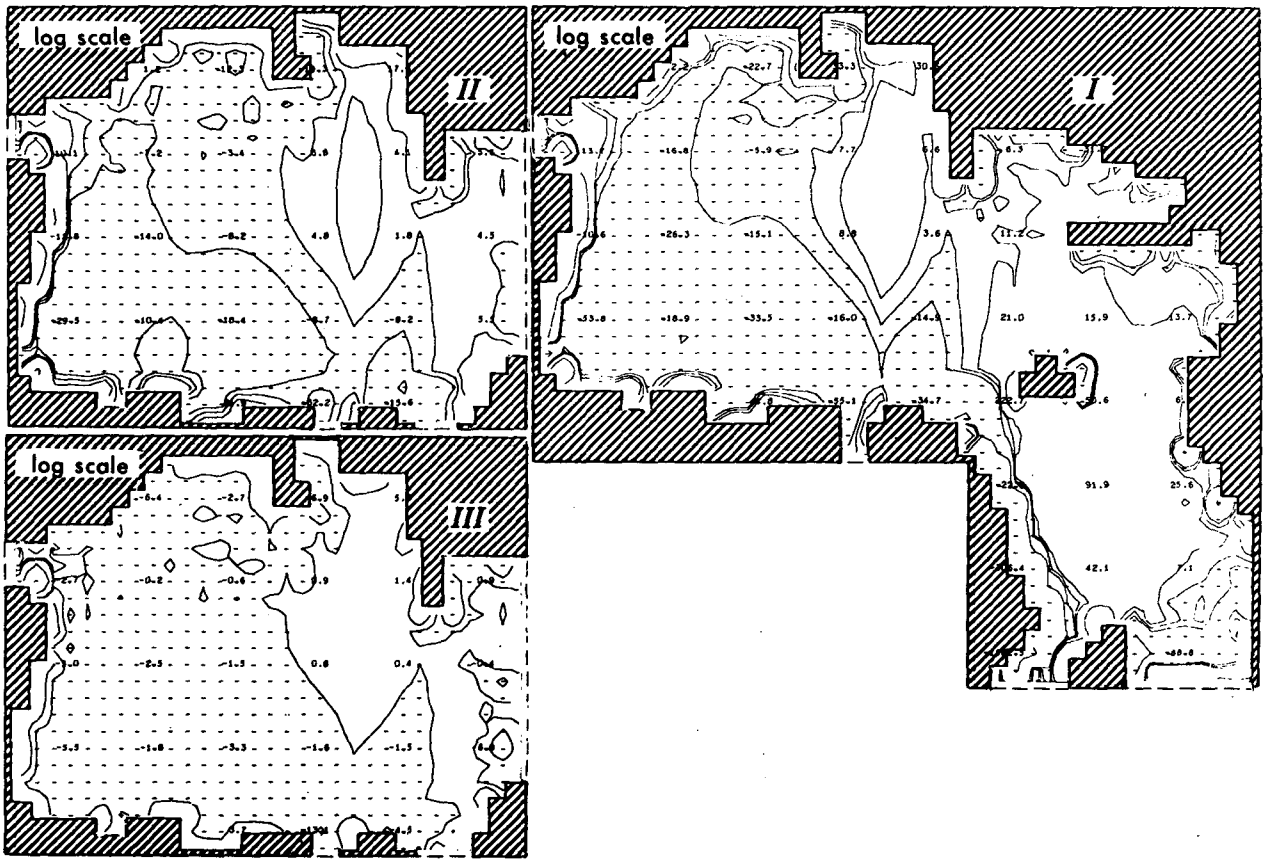

FIG. 12. Vertical velocity at 15 m with contours at 0, ±1, ±10, ... cm day^{-1}. Downward motion is predicted in the shaded area.

of the Ekman layer is very important in determining the predicted density structure of the upper Arctic Ocean. In the present model the induced vertical velocity depends primarily on local wind stress curl. This situation may or may not change very much when a realistic ice model is eventually included in Arctic Ocean studies. For example, if ice motion is similar to the steady two-dimensional motion of an incompressible, inviscid fluid [a possibility suggested by Rothrock (1973)], then the induced vertical velocity will still be proportional to local wind stress curl. On the other hand, if ice motion approximates that of a rigid body [as assumed in Hart's (1975) study], then a uniform vertical velocity will be induced in the water under the ice, dependent on the net torque exerted on the ice by a field of wind stress. In this latter case, considerably different predictions of density structure in the upper ocean might occur.

Vertical velocities take on a more complicated pattern in the deep water, as a result of the irregular topography. Insight into the overall vertical motion and its relation to the horizontal velocity field can be obtained by looking at trajectories of particles inserted into the three-dimensional flow field. Fig. 13 shows a typical path of a particle starting in the Norwegian Sea. After traveling poleward in the Norwegian Current and rising in the Barents Sea, the particle crosses the Eurasian Basin by riding a strong component of Ekman transport in the top layer. It then becomes trapped in the dominant circulation of the Beaufort Gyre, spiraling downward and outward.

Particles which start their downward spiral near the center of the Beaufort Gyre go very deep before they eventually break free of the closed circulation. Others which start near the periphery may only make a few revolutions. Fig. 14 shows an example of the latter situation. The tendency for the particle to rise eventually along the Siberian shelf and break loose from the gyre is typical. In the example shown, the particle rides the Transpolar Drift into the East Greenland Current, circles downward in the Greenland Sea, returns above the Lomonosov Ridge for a circuit of the Eurasian Basin, and finally leaves the region via the East Greenland Current.

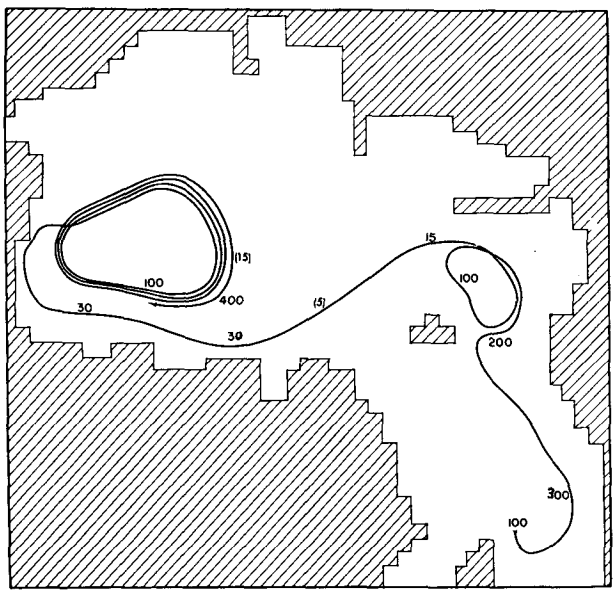

FIG. 13. A particle trajectory for Case I. Particle depth in meters is shown at representative points along the path. Time in years is shown in parentheses.

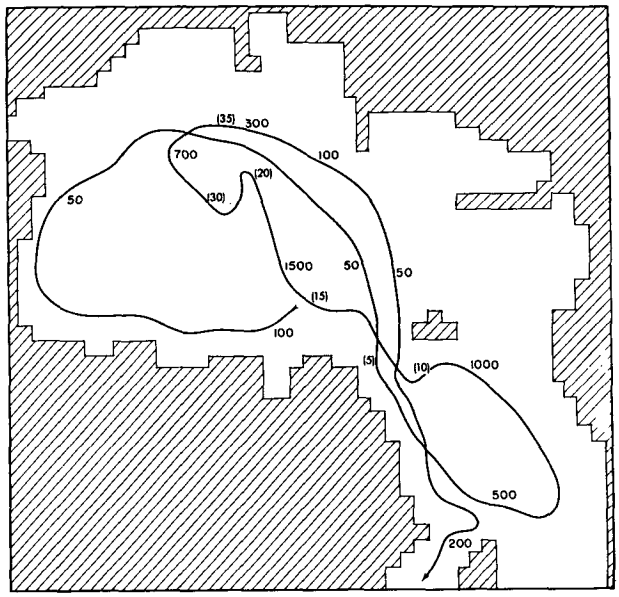

FIG. 14. A particle trajectory for Case I. Notation is as in Fig. 13.

5. Predicted salinity and temperature

Surface salinity maps for the three cases are shown in Fig. 15. These may be compared with the observed field in Fig. 16. In the Greenland Sea, a predicted tongue of high-salinity water, extending northward along the Norwegian coastline and splitting into two segments near Spitsbergen, agrees well with the observed pattern. Along the Greenland coast, low salinities are predicted, but they are not as low as the values observed. Advection of salty water from the North Atlantic and fresher water from the mid-Arctic are evidently responsible for the patterns, as has been verified by looking at the dominant terms in the salt equation.

In the Arctic Ocean, many Siberian marginal seas have very low predicted salinity as a result of river runoff. Along the Alaskan coast, where there is little runoff, an alternating series of high- and low-salinity regions appear in Cases I and II; and these may be somewhat unrealistic. High wind stress in the area and a jagged coastline produce alternations in vertical velocity and set up salinity patterns of small scale.

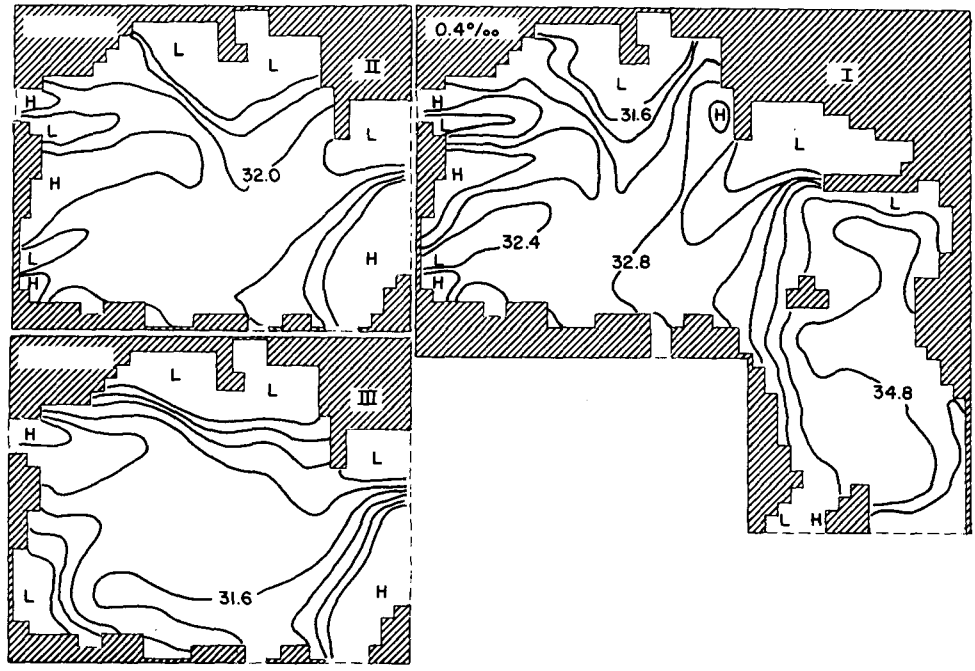

FIG. 15. Predicted surface salinity. The contour interval is 0.4‰. Contour lines are omitted from some regions of high or low salinity near coasts (denoted by H and L symbols).

Case III appears to give more reasonable results, consistent with MacKenzie River runoff and higher salinity Pacific inflow. A slight salinity maximum in Case I near Severnaya Zemlya may be a realistic response to a maximum in the wind curl nearby (see Fig. 12). High observed salinities in this portion of the Eurasian Basin have been attributed to special dynamical processes in adjacent submarine canyons by Coachman and Barnes (1962), but an explanation in terms of wind-induced vertical advection seems more straightforward.

Tongues of high and low salinity spiral inward toward the mid-Arctic in a manner consistent with the surface currents. Case III shows the best pattern relative to observations, in spite of low predicted geostrophic velocities. Transport of salt toward the center of the gyre is accomplished mainly by an Ekman drift component in the surface layer, and this component, unlike the geostrophic current, is not significantly affected by lateral friction. Mid-ocean values of surface salinity decrease as the wind stress does, probably because coastal maxima near Alaska have a reduced input into the surface water.

Predicted surface temperatures (not shown) are within 0.5°C of the freezing point (−2°C) over most of the Arctic Ocean and in the East Greenland Current. In contrast, temperatures in the Greenland and Norwegian Seas are always above −1°C, except near the Greenland coast. A warm Norwegian Current maintains temperatures above 1°C year-around all the way to Spitsbergen and the northern tip of Norway. These phenomena are consistent with observations, and indicate that the simple heat-flux boundary condition works reasonably well. In Case I, the major area of seasonal transition between temperatures near freezing and temperatures above 0°C is the Barents Sea, and this is consistent with known seasonal fluctuations in pack-ice limits.

Figs. 17 and 18 are vertical sections of predicted salinity and temperature in the Arctic Basin. The sections cross the numerical grid from left to right and pass within 55 km of the North Pole. For making an approximate comparison, Fig. 19 (from Coachman and Aagaard, 1974) shows the observed fields along a line from the Bering Strait to the Greenland Sea.

Both the observations and the predictions show the existence of an Arctic halocline. The observed depth is about 300 m, whereas Cases I, II and III give 800, 500 and 300 m. To give some idea of how the predicted halocline in Case III is maintained, Fig. 20 shows a breakdown of the horizontal surface at 175 m depth into different subregions, determined by the dominant balance in the salt equation. The regions are rather irregular on account of the complicated vertical motions associated with the rough topography. However, it is apparent that vertical advection dominates over most of the Canadian Basin. This shows the effect of downwelling of relatively fresh surface water (which itself is supplied by lateral transport of runoff toward the center of the Basin in a convergent Ekman layer). At 175 m, the central pool of fresher water receives salt by lateral diffusion from marginal areas of higher salinity. Since the diffusion coefficient $A_H = 10^7$ cm^2 s^{-1} may be somewhat high, horizontal diffusion may be taking over some of the role that might normally be played by

horizontal advection. At the margins of the Canadian Basin, a primary balance of horizontal and vertical advective terms is associated with relatively strong upwelling of deep salty water along continental slopes. Finally, in the Eurasian Basin, horizontal advective effects are more evident, particularly in the portion of the Basin near the Siberian Shelf. There, horizontal transport of fresher water from the Canadian Basin is offset by horizontal diffusion of saltier water which rises along the Barents continental slope.

The observed temperature structure in Fig. 19 shows an "Atlantic layer," with a temperature maximum at about 500 m depth, extending across the entire Arctic Basin. The three experiments are only partially successful in reproducing this feature. In Case I, where exchanges with the Greenland Sea are predicted, the model does not deliver distinct water masses at the intermediate level and at the sill depth into the Arctic Basin. Instead, a homogenized version of the two types enters in a thick wedge. A warm layer spreads across the basin at much too great a depth. This water would eventually fill the deep basins, given sufficient time for vertical diffusion to erode the slightly stable stratification. In Cases II and III, entry of two water masses is prescribed, and the situation improves somewhat. Case III has a circulation pattern at a depth of 565 m which favors spreading of the Atlantic layer, and gives a better simulation. Both cases show a deep-water temperature discontinuity of about 0.3°C across the Lomonosov Ridge (but not across the Alpha Ridge), and this is consistent with observations.

The Atlantic layer may be an especially difficult feature to simulate correctly. The temperature of this layer is nearly a passive tracer, because density gradients at low temperature are primarily due to salinity variation. Rather than seeking a certain level determined by its temperature within a fairly stable stratification and then spreading out there, the layer is in a fairly neutral environment and moves at the mercy of currents determined by other processes.

Finally, Fig. 21 shows vertical sections of salinity and temperature across the Greenland Sea. Warm, salty water in the Norwegian Current and cold, relatively fresh water in the East Greenland Current reflect the

FIG. 16. Observed summer surface salinity (‰), from Coachman and Aagaard (1974).

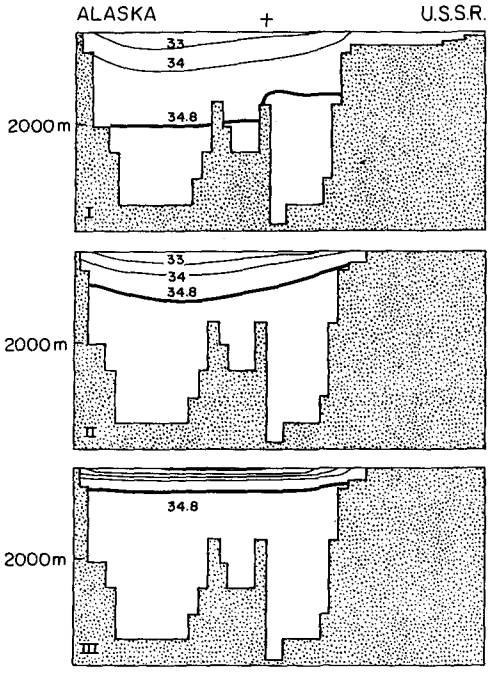

FIG. 17. Vertical sections of salinity for the three cases with contours at 31, 32, 33, 34 and 34.8‰.

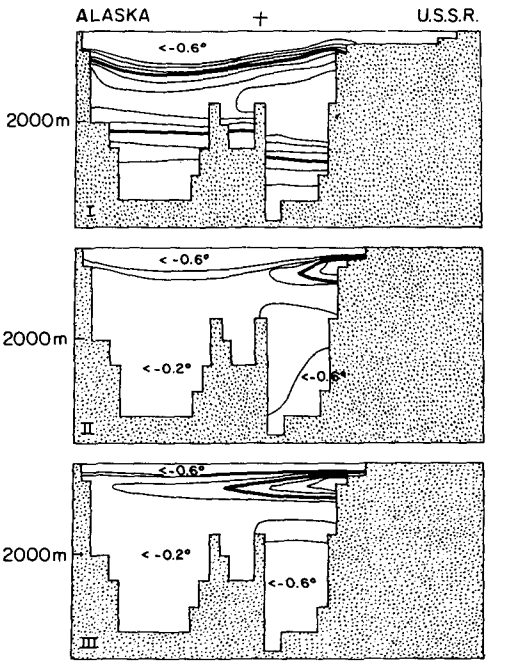

FIG. 18. Vertical sections of temperature for the three cases. The contour interval is 0.2°C, and the heavy line is for 0°C. Contour lines near the surface are left out.

respective mid-latitude and polar origins of these currents. Deep convection in the central Greenland Sea makes the entire vertical water column nearly isothermal there. Return flow from the Norwegian Current exists below the East Greenland surface flow and still shows salinity and temperature maxima, although they are considerably weakened. The latter features are too deep compared to observations, but are qualitatively correct.

6. Discussion

The numerical experiments just described are fairly successful in simulating many of the observed features of Arctic Ocean circulation. However, certain deficiencies have been noted. In particular, horizontal currents are too weak unless fairly large wind stresses are applied, but then the predicted salinity and temperature fields become less realistic. The reason for this lies in the large value used for horizontal viscosity, which was

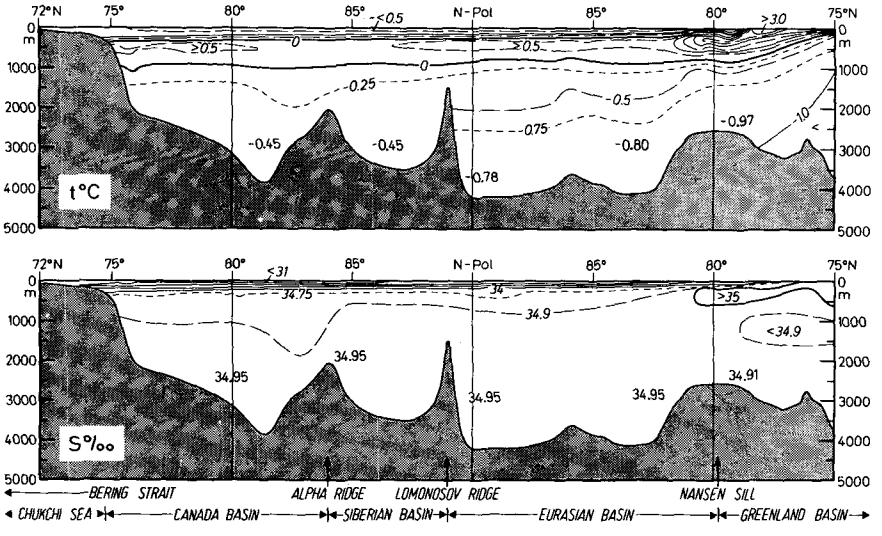

FIG. 19. Longitudinal sections of temperature and salinity across the Arctic Ocean, from Coachman and Aagaard (1974).

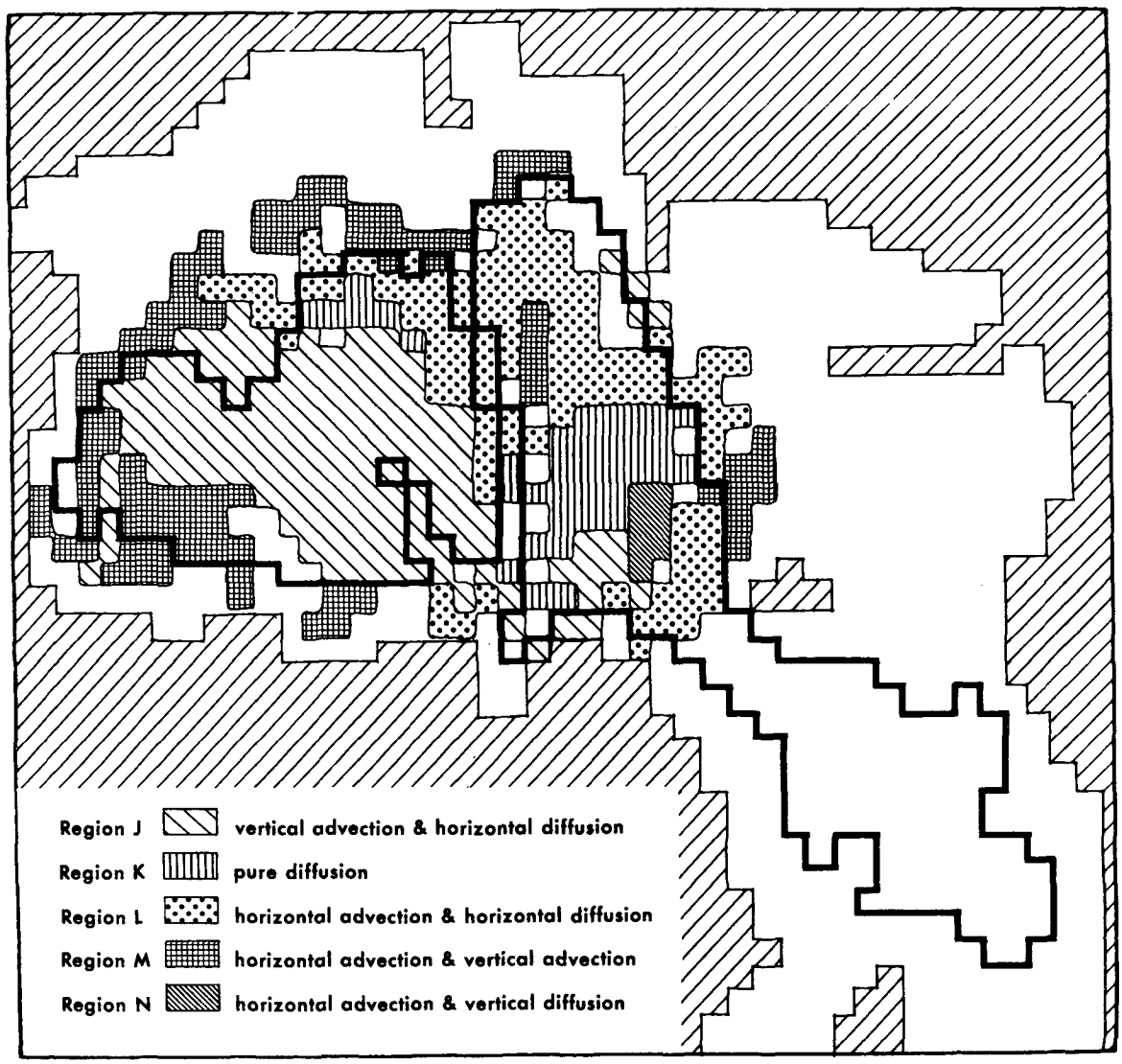

FIG. 20. Regions determined by the dominant terms in the salt equation at 175 m for Case III. (The margins of the deep basins are indicated by the heavy line.)

chosen sufficiently large to suppress computational noise.

The density field near the surface in the Arctic Basin is very sensitive to the magnitude of the vertical velocity, which depends primarily on the curl of the wind stress; and since the halocline is too deep in Cases I and II, the wind stress must be too high in those cases. For one thing, the chosen drag coefficient of 2×10^{-3}, which is admittedly somewhat high in the Greenland Sea, may also be excessive in the Arctic Basin. Stable atmospheric conditions often occur over ice-covered regions, inhibiting vertical momentum transfer and making the winds at anemometer level noticeably smaller than geostrophic winds. Also, the value of the multiplier α, which compensates for the nonlinearity of the drag law when averaged winds are used, may be too large in Cases I and II. The wind forcing on Case III is probably the most realistic.

The pattern and magnitude of horizontal currents are unrealistic unless wind stress is fairly strong, because frictional effects are too large over most of the Arctic Basin. This can be seen from Fig. 22, which shows the four largest terms in the vertically integrated vorticity equation for Case I. In this section through the center of the Beaufort Gyre, diffusion of vorticity is just as important as any of the other terms. Effects of lateral boundaries, bottom topography, and a significantly reduced β value are all noticeable. Unlike numerical experiments for mid-latitude oceans, no dominant Sverdrup balance of wind curl and planetary vorticity advection (with a resulting independence of

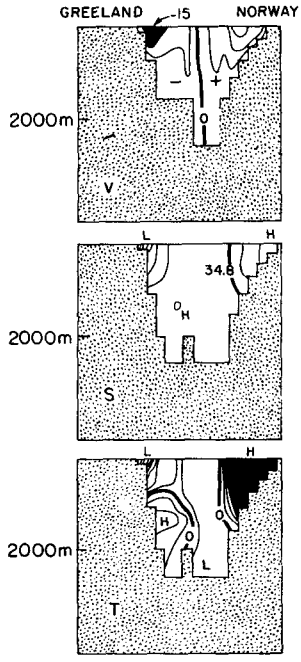

FIG. 21. Vertical sections of velocity, salinity and temperature across the Greenland Sea for Case I. The sections run along the ridge separating the deep Norwegian and Greenland Basins. Contour intervals are 2 cm s^{-1}, 0.2‰ and 0.2°C.

predicted velocities from lateral viscous effects) occurs in the interior.

The velocities in Case III are perhaps one-half as large as the observed velocities. This indicates that, although the eddy viscosity A_M is too large, it may not be absurdly large. It seems unlikely that A_M needs to be reduced by more than an order of magnitude to get realistic velocities. By reducing the horizontal grid-point spacing to 50 km, a value $A_M = 4 \times 10^7$ could be accommodated. Given sufficient computer time, such a study could be expected to give more realistic simulations of Arctic circulation. Whether the flow pattern in the Atlantic layer would change significantly is not clear. At the very least one would expect the enhanced velocities in the Atlantic layer and the improved resolution near the Greenland-Spitsbergen Passage to make the thermal structure more realistic.

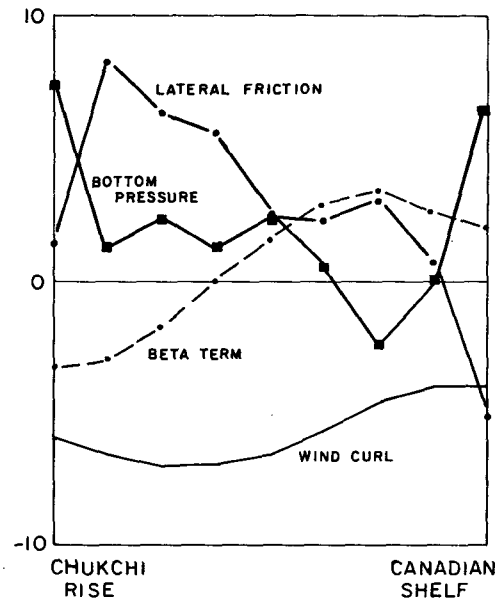

FIG. 22. The four largest terms in the vertically integrated vorticity equation for Case I. Values are in units of 10^{-4} g m^{-2} s^{-2}.

Acknowledgments. This work was carried out while the author was a student in the Geophysical Fluid Dynamics Program at Princeton University.

The author wishes to thank Kirk Bryan for his guidance and generosity. Mike Cox, Bill Holland, and many others at the Geophysical Fluid Dynamics Laboratory provided helpful suggestions. Discussions with Jerry Galt and Knut Aagaard are also acknowledged. Drafting and typing were carried out by Martha Jackson, Beverly Gladstone and Sherry Lovell. Computer time on the Princeton University IBM 360/91 was purchased via a grant from the National Science Foundation, through its Office for the International Decade of Ocean Exploration.

REFERENCES

Aagaard, K., 1969: The relationship between geostrophic and surface winds at Weather Ship M. *J. Geophys. Res.*, **74**, 3440–3442.

——, 1970: Wind-driven transports in the Greenland and Norwegian Seas. *Deep-Sea Res.*, **17**, 281–291.

Bryan, K., 1969: A numerical method for the study of the circulation of the world ocean. *J. Comput. Phys.*, **4**, 347–376.

——, and M. D. Cox, 1972: An approximate equation of state for numerical models of ocean circulation. *J. Phys. Oceanogr.*, **2**, 510–514.

——, S. Manabe and R. Pacanowski, 1975: A global ocean-atmosphere climate model. Part II. The oceanic circulation. *J. Phys. Oceanogr.*, **5**, 30–46.

Budyko, M. I., Ed., 1963: *Atlas of the Heat Balance of the Earth.* Gidrometeoizdat, Moscow, 69 pp.

Campbell, W. J., 1965: The wind-driven circulation of ice and water in a polar ocean. *J. Geophys. Res.*, **70**, 3279–3301.

Coachman, L. K., and K. Aagaard, 1966: On the water exchange through Bering Strait. *Limnol. Oceanogr.*, **11**, 44–59.

——, and ——, 1974: Physical oceanography of Arctic and sub-Arctic seas. *Arctic Geology and Oceanography*, H. Nelson and Y. Herman, Eds., Springer-Verlag, 1–72.

——, and C. A. Barnes, 1962: Surface water in the Eurasian Basin of the Arctic Ocean. *Arctic*, **15**, 251–277.

——, and ——, 1963: The movement of Atlantic water in the Arctic Ocean. *Arctic*, **16**, 8–16.

Dietrich, G., 1960: Temperatur-, Salzgehalts- und Sauerstoff-Verteilung auf den Schnitten von F.F.S. *Anton Dohrn* und V.F.S. *Gauss* im Internationalen Geophysikalischen Jahr 1957/1958. *Deut. Hydrogr. Z.*, Reihe B, 4, 103 pp.

Dunbar, M., and W. Wittman, 1963: Some features of ice movement in the Arctic Basin. *Proc. Arctic Basin Symposium*, October 1962, Arctic Inst. North America, Washington, D. C., 90–104.

Fel'zenbaum, A. I., 1961: The theory of steady drift of ice and the calculation of the long period mean drift in the central part of the Arctic Basin. *Problems of the North*, **2**, 13–44.

Fletcher, J. O., 1965: The heat budget of the Arctic Basin and its relation to climate. RAND Corp. Rept. R-444-PR, Santa Monica, 179 pp.

Galt, J. A., 1973: A numerical investigation of Arctic Ocean dynamics. *J. Phys. Oceanogr.*, **3**, 379–396.

Hart, J. E., 1975: The flow of a two-layer fluid over topography in a polar ocean. *J. Phys. Oceanogr.*, **5**, 615–624.

Holland, W. R., 1971: Ocean tracer distributions: Part I, A preliminary numerical experiment. *Tellus*, **23**, 371–392.

Kraus, E. B., 1972: *Atmosphere-Ocean Interaction*. Oxford University Press, 275 pp.

Lvovitch, M. I., and S. P. Ovtchinnikov, 1964: *Physical-Geographical Atlas of the World*. Academy of Science USSR and Central Administration of Geodesy and Cartography, USSR, Moscow, 298 pp.

Maykut, G. A., and N. Untersteiner, 1969: Numerical prediction of the thermodynamic response of Arctic sea ice to environmental changes. RAND Corp. Memo. RM-6093-PR, Santa Monica, 173 pp.

Palfrey, K. M., Jr., 1967: Physical oceanography of the northern part of the Greenland Sea in the summer of 1964. M.S. thesis, University of Washington, 52 pp.

Rooth, C. G., and H. G. Östlund, 1972: Penetration of tritium into the Atlantic thermocline. *Deep-Sea Res.*, **19**, 481–492.

Rothrock, D. A., 1973: Circulation of an incompressible ice cover. *AIDJEX Bull.*, No. 12. University of Washington Division of Marine Resources, 61–68.

Semtner, A. J., 1973: A numerical investigation of Arctic Ocean circulation. Ph.D. thesis, Princeton University, 251 pp.

——, 1974: An oceanic general circulation model with bottom topography. Numerical simulation of weather and climate. Tech. Rept. No. 9, University of California, Los Angeles, 99 pp.

——, 1976: A model for the thermodynamic growth of sea ice in numerical investigations of climate. (Submitted for publication.)

Smith, S. D., 1970: Thrust-anemometer measurement of wind turbulence, Reynolds stress, and drag coefficient over the sea. *J. Geophys. Res.*, **75**, 6758–6770.

Smith, S. M., H. W. Menard and G. Sharman, 1965: World-wide ocean depths and continental elevations averaged for areas approximating one degree squares of latitude and longitude. Scripps Inst. Oceanogr. Ref. Rept. 65-8.

Sverdrup, H. U., M. W. Johnson and R. H. Fleming, 1942: *The Oceans*. Prentice Hall, 1087 pp.

Timofeyev, V. T., 1963: Interaction of waters from the Arctic Ocean with those from the Atlantic and Pacific. *Okeanologiya*, **3**, 569–578 (English translation).

U. S. Navy Hydrographic Office, 1958: *Oceanographic Atlas of the Polar Seas. Part II, Arctic*. H. O. Publ. No. 705, 149 pp.

Vowinckel, E., and B. Taylor, 1964: Evaporation and sensible heat flux over the Arctic Ocean. AFCRL Rept. No. 64-272, McGill University.

Welch, C. S., 1972: On the calculation of wind stress curl over open ocean areas from synoptic meteorological data with applications to time dependent ocean circulation. Woods Hole Oceanogr. Inst. Tech. Rept. No. 2-6, 189 pp.

Worthington, L. V., 1970: The Norwegian Sea as a mediterranean basin. *Deep-Sea Res.*, **17**, 77–84.